Shahrood University of Technology

Journal of Mining and Environment (JME)

Journal homepage: www.jme.shahroodut.ac.ir

Iranian Society of Mining Engineering (IRSME)

Application of Remote Sensing in Lithological Mapping of Umm Tawat Precambrian Rock Assemblage, North Eastern Desert, Egypt

Kamar Samir*, Mohamed El-Sharkawi, Ahmed Niazy El-Barkooky, and Mohamed Saleh Hammed

Geology Department, Faculty of Science, Cairo University, Egypt

Article Info

Received 17 March 2023
Received in Revised form 3 April 2023
Accepted 13 April 2023
Published online 13 April 2023

DOI:10.22044/jme.2023.12857.2333

Keywords

Remote Sensing
Lithological Discrimination
Hammamat Sediments
Umm Tawat

Abstract

The Precambrian rock assemblages of Umm Tawat area in the North Eastern Desert of Egypt have a distinctive ENE-trending exposure of Hammamat sediments (HS) between the Gebel Gattar granitic pluton and the volcanoclastic succession of Gebel El Dokhan. The present work applies the Landsat-8 data and image processing techniques such as spectral signature, principal component analysis, decorrelation stretch, and band ratios to map the various Precambrian rock units and the lithofacies of the HS and their geological contacts. The recognized mappable units of this assemblage are fully identified by their spectral signature, field verification, lineament analysis, and petrographic description. The resultant high-resolution lithological map based on the maximum likelihood algorithm demonstrates ten fully discriminated mappable units of younger granitoid and HS lithofacies units besides the Dokhan volcanics and metagabbro-diorite rock units. The identified five HS lithofacies units are brownish gray conglomerate and sandstone HSf1, a green conglomerate with dominant volcanic fragments HSf2, fine-grained sediments of graywacke and silty-mudstone HSf3, interbedded conglomerates and siltstone with uranium enrichments related to the intrusive contact HSf4, and thermally metamorphosed pelitic sediments HSf5. Remote sensing techniques have been applied for the first time to reveal detailed facies variation of the Hammamat sediments of Umm Tawat. Finally, the results aforementioned above are imported to the Arc GIS database to update the geologic map with precise rock unit boundaries.

1. Introduction

Application of the remote sensing (RS) data and their image processing techniques have been considered as an important tool in geological mapping and discrimination of the various lithologies, mineral exploration, and hydrothermal alteration zones [1–7]. The lithological mapping of complex geologic terrains of the Middle East, Africa, and India was used as a variety of RS techniques [4, 8, 9]. Several studies in Egypt have applied image processing techniques of RS data to identify and characterize the Precambrian serpentinites, ophiolitic, molasse sediments, granitic rocks, and metavolcanic [10, 11, 20, 12–19]. Other investigations have also been effective in lithologically identifying Precambrian Hammamat sediments and Phanerozoic sedimentary rock units using the same approaches [21–23].

The basement rocks of Egypt are a part of the Neoproterozoic Arabian-Nubian Shield (ANS). The ANS is a juvenile continental crust formed by magmatic arc accretion through a progression of subduction, accumulation, and crustal thickening procedures through the late Precambrian Pan-African Orogeny [24–27]. In the final stage of the Pan-African evolution during the late Cyrogenian-Ediacaran age (650-550 Ma), the Egyptian basement complex was accompanied by the eruption of Dokhan volcanics, deposition of molasse-type sedimentary rocks known as Hammamat sediments (HS), and the emplacement of felsic intrusions [26, 28–31]. The Eastern Desert of Egypt represents the northwestern of the ANS, and has been distinguished by [32] into three distinctive litho-tectonic domains: the North, Central, and Southern Eastern Deserts (NED, CED,

* Corresponding author: moonsamir9@cu.edu.eg (K. Samir)

SED). The NED includes the studied area, and is characterized by the abundance of Ediacaran non-metamorphic volcano-sedimentary successions including interfingering Dokhan volcanics, HS, and abundant post-tectonic granitoid with different gneissic varieties, and one of the largest dyke swarm systems [25, 31, 33].

On general geologic maps of Egypt, the HS and younger granites account for approximately 80% of the Precambrian basement rocks in the NED of Egypt [31, 34–36]. The HS were previously mapped as an undifferentiated unit regardless of their facies variation [34, 37, 38]. To the contrary, the Egyptian younger granites have been intensively classified based on field relations, geochemical, petrographical, and radiometric background characteristics [39–44].

The main objective of the current study is facies discrimination and lithological mapping of HS and granites and delineating the structure of the Umm Tawat area in the NED of Egypt utilizing different processed remote sensing data and high-resolution Google Earth images aided with field verification.

2. Geologic Setting

The Umm Tawat area is located in the southern portion of the NED of Egypt between latitudes 27° 05' and 27° 10' N and longitudes 33° 10' and 33° 23' E, to the west of Hurghada (Figure 1a). It is covered by the Precambrian assemblages including the intrusive rocks, Neoproterozoic volcanic rocks, and Hammamat molasse sedimentary rocks that are bounded by Gebel Gattar and Gebel El Dokhan (Figure 1b). The intrusive rocks include metagabbro-diorites and younger granites. The metagabbro-diorites (MD) represent the oldest rocks in the area of investigation. They are of limited exposure, and occur as small dark gray hillocks. The Dokhan volcanics (DV) erupted before the younger granites in the north part of the studied area (Figure 2a). It dates back to 592 Ma utilizing Rb-Sr technique [31] with complete matching with the age (593 + 13 Ma) measured by the 206Pb/238U method [45]. This thick sequence of volcanics is composed of high-K calc-alkaline lava flows and pyroclastics of predominantly andesitic to rhyolitic composition with imperial porphyry [37].

The most predominant outcrop observed in the studied area is the HS. It is composed mainly of immature to sub-mature clastic rocks of molasse facies sediment [46]. Herein, these HS are known as Umm Tawat sediments (Figure 2a), and consist of conglomerate, wacke, and siltstone [35]. According to [47], the HS of the Eastern Desert have been deposited in three tectonic settings: the first stage is deposited in pre-collision as fore-arc, intra-arc, and back-arc basins, the second stage is deposited during the syn-collision stage as fore-arc basins and low land basins in the accretionary prism, and the third stage during the late collision as a low land and intramontane basins. The sediments of each stage are distinguished by the shape and type of the basin and the source of sediment supply. To the contrary, [31] ported that the area is a part of the late Neoproterozoic crustal evolution that culminated in a major extensional event, escorted by bimodal igneous activity, and deposition of terrigenous clastic sediments. The HS of Umm Tawat are subjected to regional compressional deformation that forms G. Umm Tawat and a N47°E regional open anticline fold plunges 5° toward the SW direction [48].

The major intrusive bodies in this area are mainly affiliated with the Younger pink Granites of [36]. The huge and complex granitic plutons of G. Gattar and Sala`at El Bali intrude the HS at the eastern and southern parts of the studied area. Both plutons have U dates 579 and 583 Ma age by zircon model age [31] Gattar granite shows intrusive contact with HS forming offshoots and tongues to HS and subsequently affected by SE-dipping thrusts (Figure 2b). The associated uranium mineralization along the Gattar granite contact with the HS and their dissecting faults has been documented and extensively exploited by the nuclear material authority of Egypt since the seventieth. In a similar geologic condition, [49] demonstrated that there are strong spatial and thermal relationships between the location of hydrothermal mineral deposits related to fluid flux mechanisms of porphyry Cu formation and the existing point and line features as intrusive contacts, fault density, fault intersections, and proximity to faults, and can help mineral exploration and prospectivity.

The whole rocks in the studied area are dissected by a system of dikes (swarm). These dikes are basic to acidic in composition, closely associated with granitoid (Figure 2c), and intruded under extensional conditions in the Eastern Desert and Sinai Peninsula [32, 50, 51].

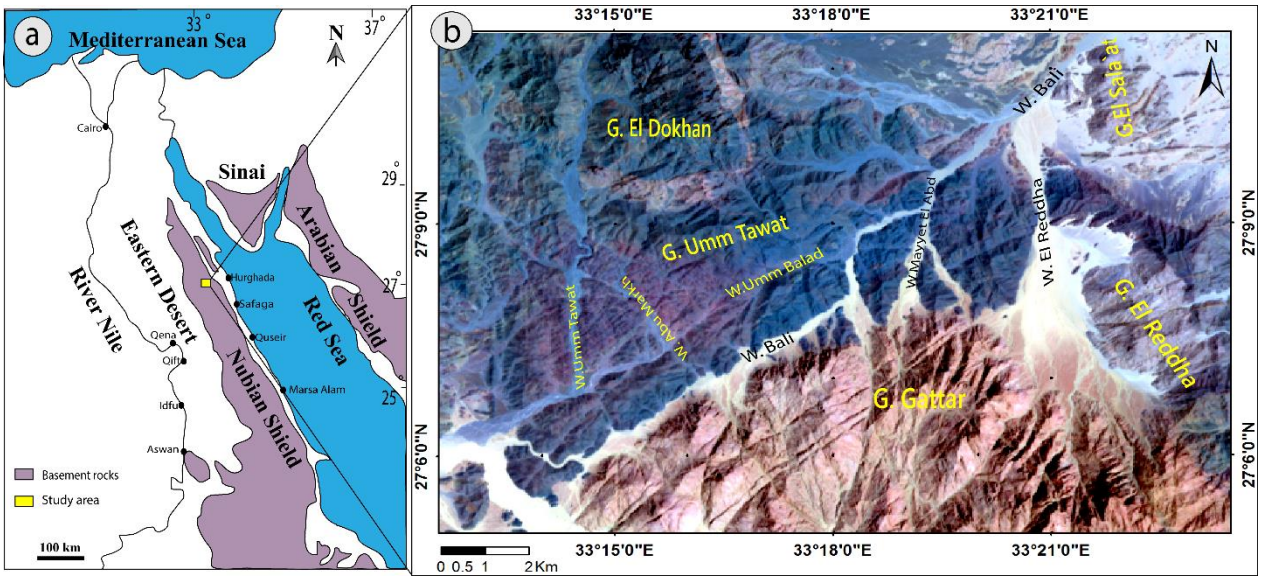

Figure 1. (a) Location map of the studied area (yellow box) in the Eastern Desert. (b) Landsat image of the Umm Tawat area.

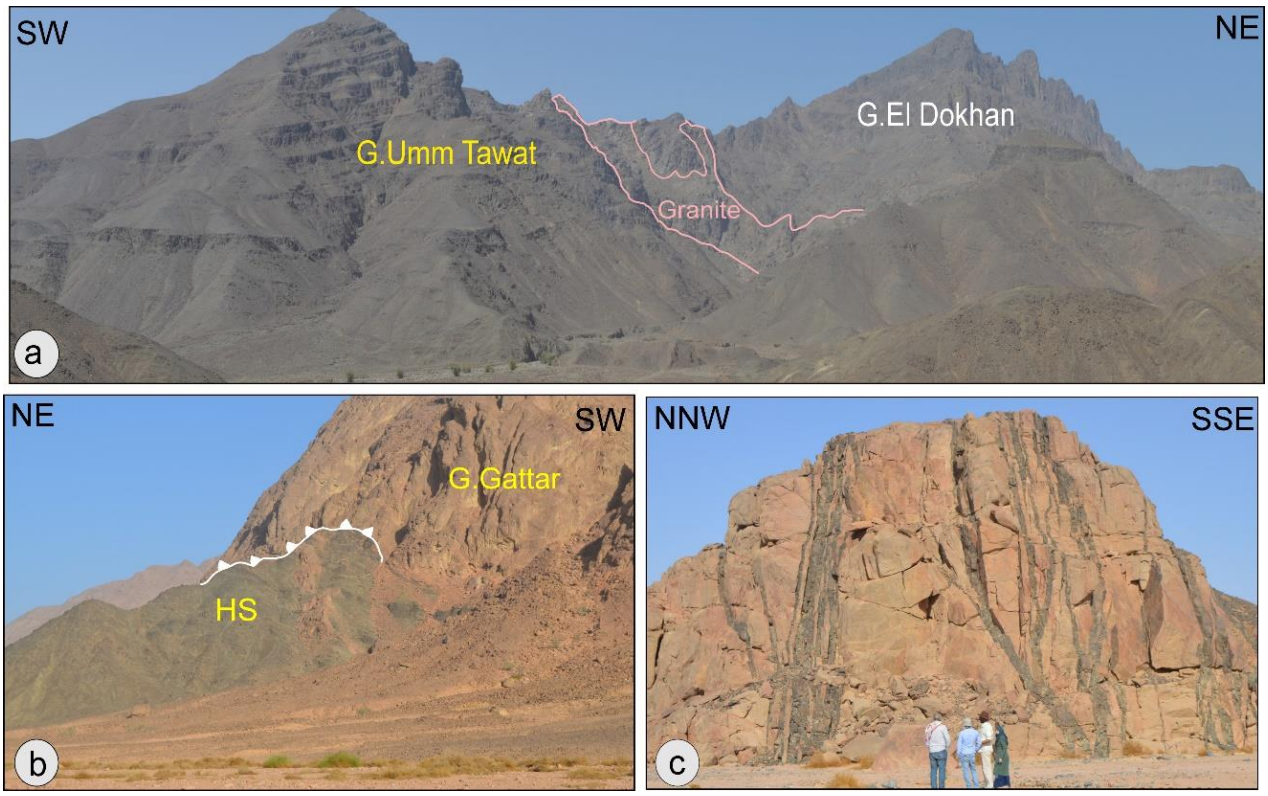

Figure 2. Field photographs of the studied area showing (a) G.Umm Tawat southwest of G. El Dokhan that they intruded with younger granites. (b) Intrusive contact of pink granite of G. Gattar with Hammamat sediments (HS) and dipping thrust faults toward Gattar. (c) Dike swarm cut younger granite.

3. Dataset and Methods

3.1. Landsat-8 OLI

Landsat-8 mission was launched in February 2013 from California, and is yet operating. It is carrying a two-sensor payload, the Operational–Land Imager (OLI) that collects image data for nine visible, near-infrared short-wave infrared bands, and two long-wave thermal bands are recorded. It provides a spatial resolution of 15 m for the panchromatic band, 30 m for VNIR and SWIR bands and 100 m for the TIR bands.

The Landsat-8 sight (Path 175/Row 41) UTM projection of Z 36 North and WGS-84 datum was acquired in April 2017 with ID LC81750412017107LGN00. This data covering the studied area was obtained through the U.S.

Geological Survey (USGS) and prepared for digital image processing using the ENVI 4.8, ArcGIS10.3, and ILWES 3.3 softwares.

3.2. Pre-processing

The main pre-processing steps include atmospheric correction, removing the unwanted noise, and re-scaling the raw radiance data from the imaging spectrometer to reflectance data. By using the FLAASH algorithm correction tool, the data was calibrated to spectral radiance, and converted from the digital number (DN) to reflectance.

3.3. Digital image processing techniques

Several enhancement techniques were used in this work including spectral signature analysis (SSA), band ratio (BR), principal component analysis (PC), decorrelation stretch (DS), and supervised classification, as revealed in the flowchart (Figure 3a).

The PC analysis was used to compress bands of redundant data to be compacted into fewer bands of high variance data, while the DS applies a contrast stretch to the principal components of an image. Also it is a technique used to remove the high correlation commonly found in multi-spectral datasets.

In addition, the spectral signature profiles are applied to identify each lithological unit exposed in the studied area (Figures 3b & 3c), and it represents the fundamental criteria for selecting the band ratios transformation. The spectral profile of the studied area shows the general reflection and absorption differences for all bands; thus the different ratios of these bands will be a significant discrimination tool. The producing profile in this study reveals that the majority of the exposed lithological units exhibit a weak reflectance reaction at bands 1 and 2 and a moderate absorption at band 7. In contrast, the exposed lithological units exhibit an increasing spectral reflectance action at bands 3 and 4 reaching maximum in some lithologies in band 5 and the majority in band 6. The BR technique was applied to improve spectral diversities between various targets as a highly produced DN ratio [52]. Different BR images were proposed by different authors, and have been used effectively to enhance lithological mapping as an example; (4/7,3/4,2/1) RGB) ASTER image by [10] to map the Allaqi Suture units in the SED of Egypt, [53] used (7/6, 6/5, 6/4) band ratio for the mapping of gneiss domes in south Tibet, and (4/5, 5/7, 3/1 RGB) Landsat 8 was proposed by [16] for lithological mapping of Esh El Malaha area, Egypt, in addition to [3] that applied band ratio (7/5,7/6,5/3RGB) of Landsat 8 in Meatiq area of Egypt. Furthermore, new band ratios (6/5,5/4,4/3 RGB), (4/2,6/5,(7+6)/4 RGB) were proposed in the present work based on SSA.

Eventually, utilizing supervised classification is a sort of information clustering of the pixels into classes based on training sites (ROI) introduced by the user [54, 55]. Many different algorithms are available for supervised classification; in this paper, the maximum likelihood has been tested. It was found to be the most accurate and commonly used classifier when data is satisfied with the distribution default [56].

3.4. Lineament extraction

Lineaments are defined as any simple or composite and mappable linear features that concern the geologic and geomorphological lineaments [eg. 57, 58]. The geological lineaments such as faults, joints, fractures, or lithological boundaries[59]. Lineaments extraction from RS data can be accomplished through automatic via suitable software applications or by manual vision and extraction [59, 60]. The automated lineament extraction was performed in the current study utilizing the PCI-Geomatica 2017 software. Enhancement image techniques are regarded as one of the most important stages in lineament extraction [61]. The PC1 of principal component analysis from OLI data was induced in this software to extract lineaments as it carries the most information.

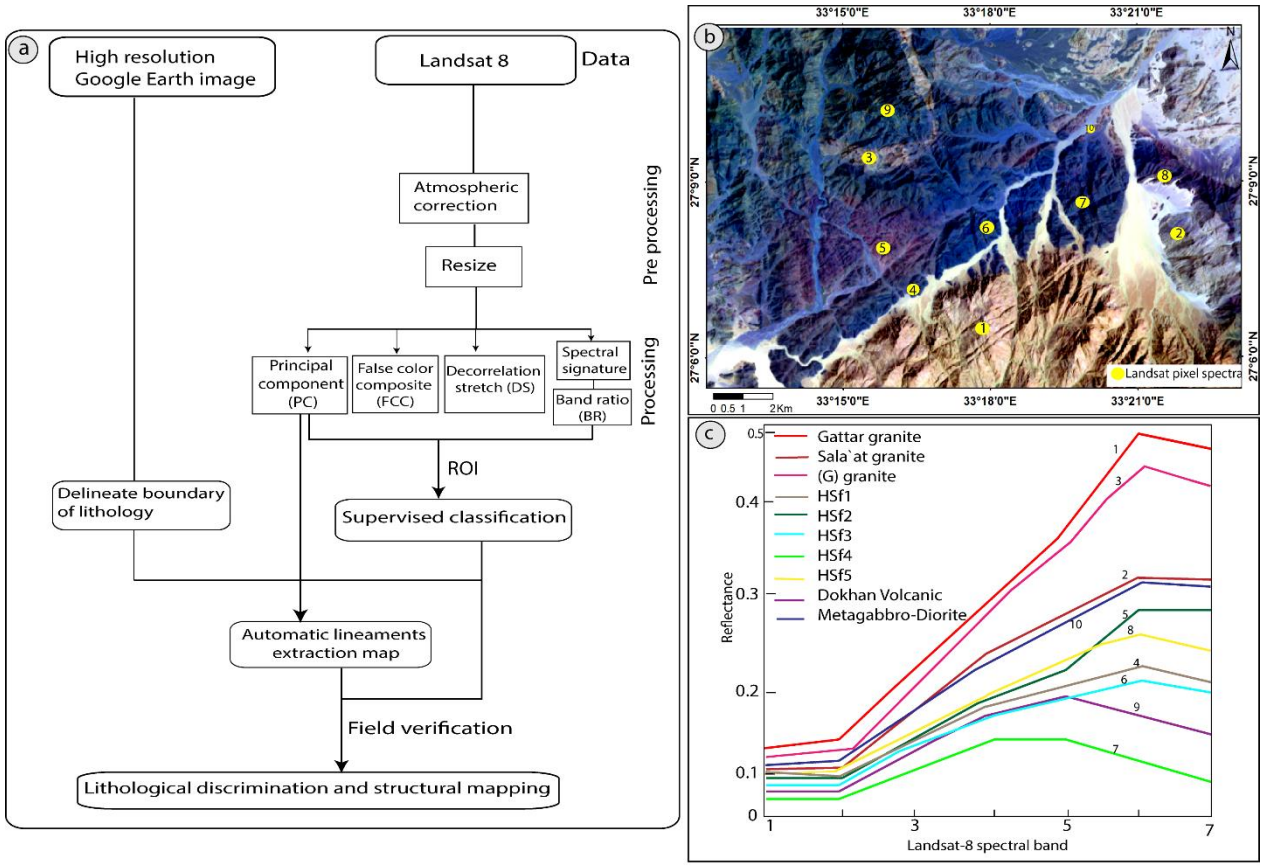

Figure 3. (a) Flow chart showing the steps of image pre-processing and processing in the present work. (b) Color composite image (7,5,1 RGB) of Landsat-8 showing the position of the pixel related to spectral in c. (c) Spectral Signature profile of the rocks in the study area by Landsat 8 data.

4. Results and Discussion

4.1. Lithological discrimination

The application of various RS image processing in the Umm Tawat area gave the best results for discriminative lithological rock units. Regarding to decorrelation stretch, the (2, 4, 7 RGB) best FCC image for differentiating between two phases of younger granites and two various facies in HS (Figure 4a). The analyses of the eigenvector PC values enable us to give a concept about the band composites selection that enhanced the variance color among the rocks. The eigenvalues (Table 1) display high positive value, high negative value, and near zero indicating the correlation of the original bands data. The first three PC bands would be used for lithological mapping [1] that contain here about 99.88% of the variance. PC1 contains one of the most variance data 95.10%, dominated by brightness differences caused by topographic differences and slope directions, PC2 explains 4.49% variance, and PC3 accounts for 0.29%. The other PC bands seem to be noisy because they contain low volumes of variance data. Dependent on these results of the PC analysis, the best RGB composite images of maximum lithological discrimination are developed (PC1, PC2, PC3, Figure 4b), showing several distinguishing features such as younger granites (Gattar granite and Sala`t El Bali granite), DV, MD, and HS. The DV is shown in orange color, MD is displayed in violet color, HS are exhibited in four colors so that they are initially divided into four facies (HSf); HSf2 shows hues of a mauve purple, HSf3 shows yellow, HSf4 appears in the southern part of HS as a pinkish yellow. HSf5 shows pink slightly as in the first facies but differs in SSA, while younger granites are displayed alternately in dark and light pinkish-blue.

The PC techniques are also useful in the detection and recognition of the structure and boundary between different facies and units in the studied area. Two regions have been studied (Figure 4b) showing the gradational in color between HSf2, HSf4, and DV that indicates a gradational boundary between these units at A region and also illustrates the strike-slip movements between the dikes (Figure 4b). Another region (B) reveals nearly irregular contact of HSf4 between HSf2 and HSf3 (Figure 4b).

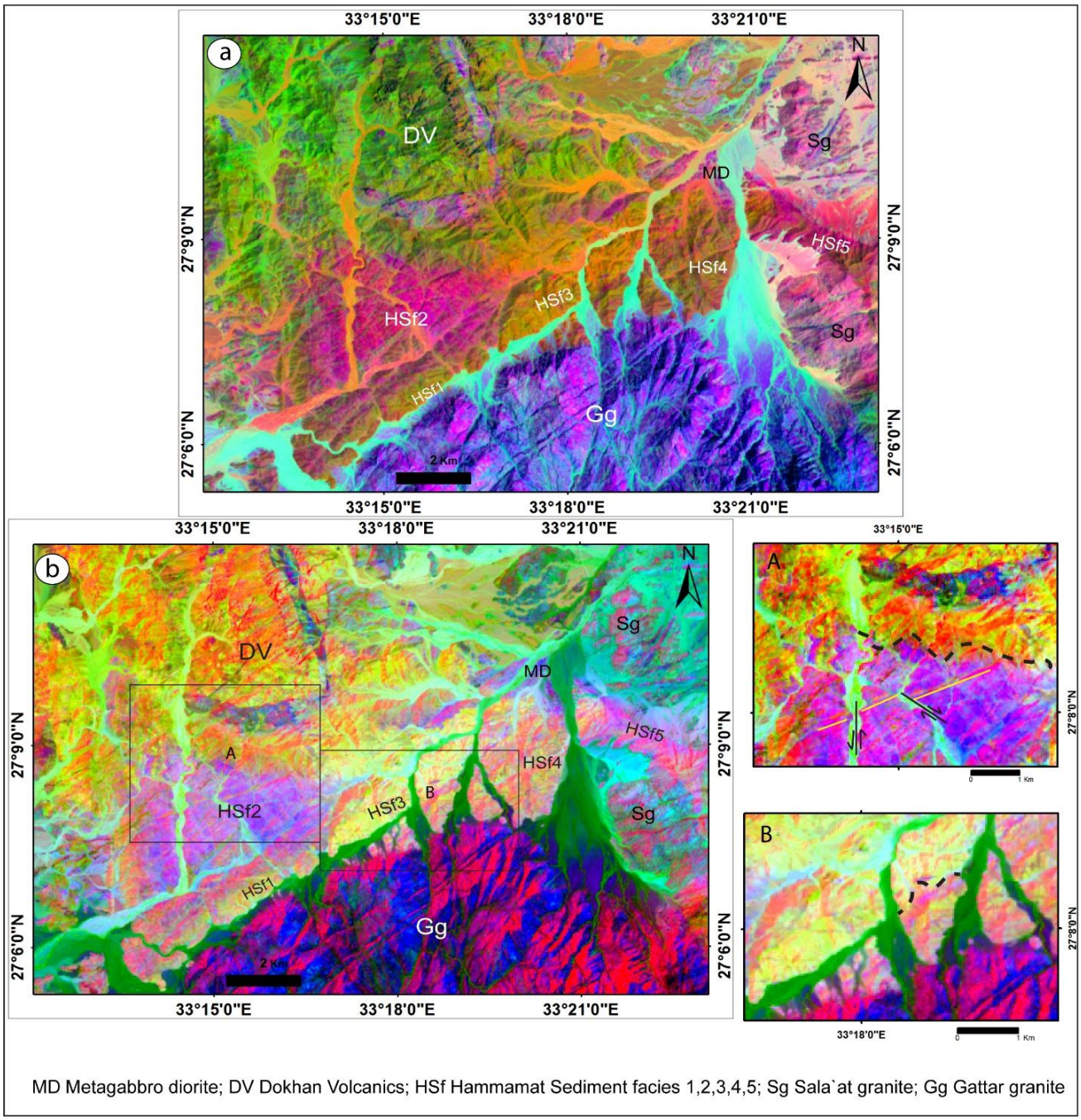

Figure 4. (a) Decorrelation stretch 2,4,7 for RGB image. (b) Principal component analysis PC1, PC2, PC3 in RGB with two selected regions for detailing the contact and structure (A) region shows gradational contact between HSf1 and DV, NNE dextral and NW sinistral strike-slip faults along wadies, (B) region reveal irregular contact between HSf2 and HSf3.

Table 1. Principal component analysis of Landsat OLI bands.

Eigenvector	b1	b2	b3	b4	b5	b6	b7	Variance %
PC1	-0.132	-0.149	-0.233	-0.369	-0.437	-0.541	-0.535	95.10
PC2	0.351	0.373	0.440	0.388	0.218	-0.354	-0.469	4.49
PC3	0.422	0.419	0.269	-0.340	-0.561	-0.023	0.378	0.29
PC4	0.075	0.096	0.095	-0.238	-0.109	0.747	-0.589	0.06
PC5	0.272	0.259	-0.303	-0.598	0.628	-0.114	0.008	0.03
PC6	-0.464	-0.133	0.736	-0.417	0.196	-0.092	0.052	0.03
PC7	-0.620	0.753	-0.190	0.087	-0.049	0.008	-0.002	0.0

The previously proposed band ratio can distinguish between the various lithological rock assemblages identified in the studied area. By applying them, they produced the following results:

The band ratio (4/7,3/4,2/1 RGB) ASTER image produced by [10] that is equivalent to (5/7, 4/5, 3/1 RGB) in Landsat 8 can separate three facies within HS with their yellow, green, yellowish-green while the granite appears as blue color (Figure 5a). Using Wolter`s band ratio (7/6,6/5,6/4 RGB), characterizes five variant facies in the HS and discriminates the Gattar granite from other granites found in the studied area. However, it does not differentiate one of the facies of HS as orange in color from other granites but the HSf4 is sub-divided into two different colors that reflect sub-facies as HSf4a for a light green color (Figure 5b). Applying [16] band ratio 4/5,5/7,3/1 RGB (Figure 5c) gives variant facies of the molasse sediment as yellow and orange color and display violet color for all types of granite. [3] applied band ratio (7/5,7/6,5/3RGB) of the OLI, donating better results in the differentiation of the HS facies, DV, and Gattar granite but did not recognize other types of granite (Figure 5d).

The spectral signature of Landsat 8 in the Umm Tawat area shows a variance in reflectance behavior between different lithologies and bands (Figure 2c). The spectra of the younger granites show maximum reflectance (0.3-0.5) in band 6 (b6), where the dominant mineral composition is alkali feldspars and biotite. The SSA shows high different reflectance between b6 and b5 with high absorption in b5 at HSf2 and HSf5 sediments. Further, the reflectance is similar in b4 and b5 with low absorption in b6 at HSf3, and HSf4 indicating a high clay mineral [62], so the following band ratios (6/5,5/4,4/3 RGB), and (4/2,6/5,(7+6)/4 RGB) were tested.

Band ratio (6/5, 5/4, 4/3 RGB) is the best to discriminate between different granites types as shown in buff color for the G. Gattar granite and light green color for the granite of G. El Reddah and G. El Sala`at, mixed light buff-green color in granite (G) that offshoot DV, and small restricted area of metagabbro-diorite northeast of the area. In addition, it differentiates the facies of sediments; that show HSf1 dark brown color, HSf2 a light brown color, HSf3 dark green, HSf4 dark brownish-green color along with the granitic intrusion, and HSf5 view as a reddish brown (Figure 5e). Also the band ratio 4/2, 6/5, (7+6)/4 RGB is confirmed for the separation of the volcanic as well as the granite and the HS (Figure 5f).

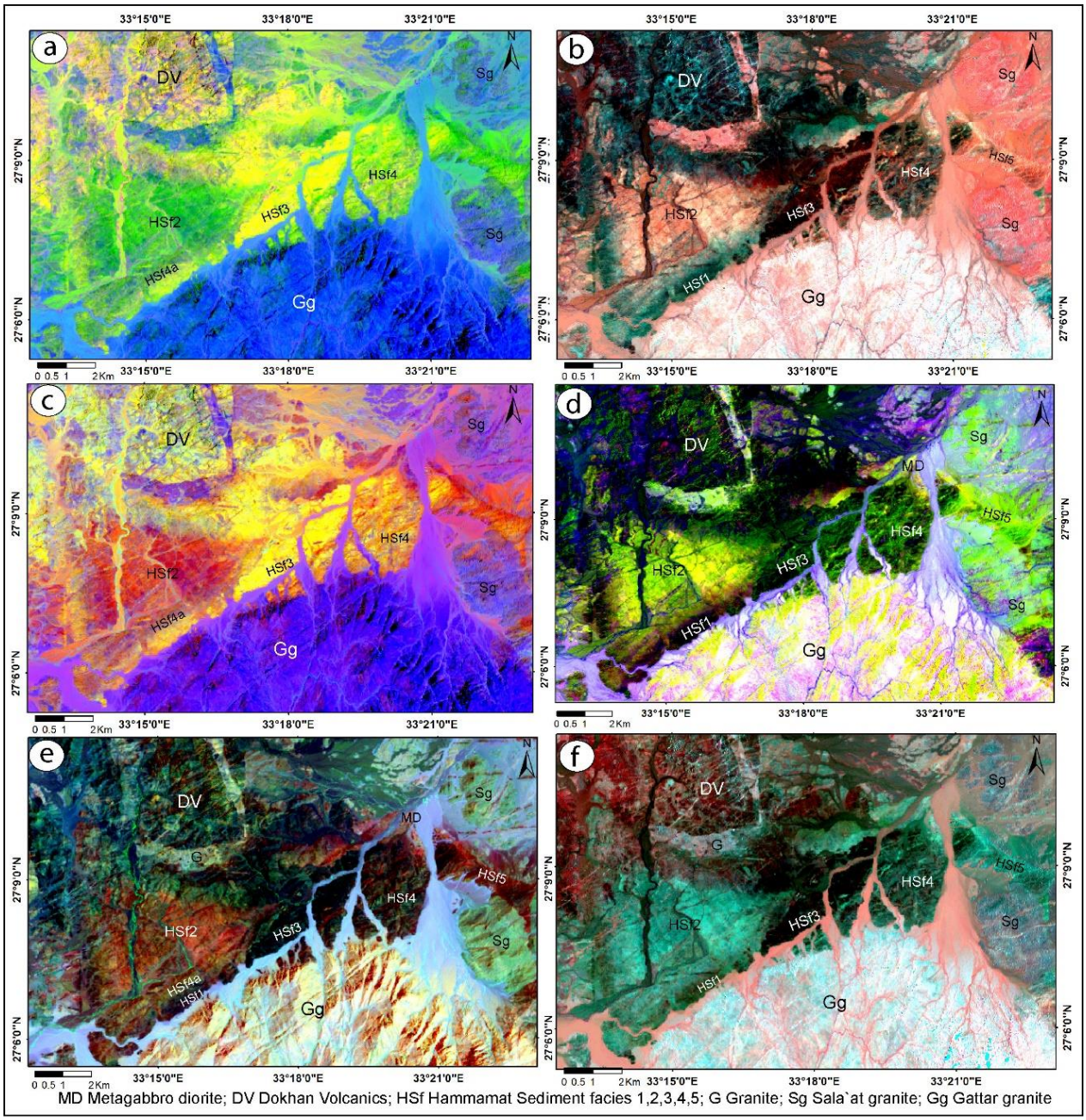

Figure 5. Band ratio images (a) 5/7, 4/5, 3/1 RGB [10] (b) 7/6, 6/5,6/4 RGB[53]. (c) 4/5, 5/7, 3/1 RGB [16]. (d) 7/5,7/6,5/3 RGB [3]. (e,f) Band ratios (6/5,5/4,4/3 RGB) and (4/2,6/5,(7+6)/4 RGB) of the present work, respectively.

The maximum likelihood classification was produced with overall accuracy (83%), and the kappa coefficient (0.82). Well-represented training sites (ROI) were detected for ten different exposed lithologies and the Wadi deposits in the studied area excluding the training site of dikes. Therefore, there is some heterogeneity in colors especially in the western part due to the many dikes that have been dissected in the area. It distinguished ten classes into ten colors, corresponding to certain rock units (Figure 6) that gave a better exclusion for the assemblage of the basement rocks.

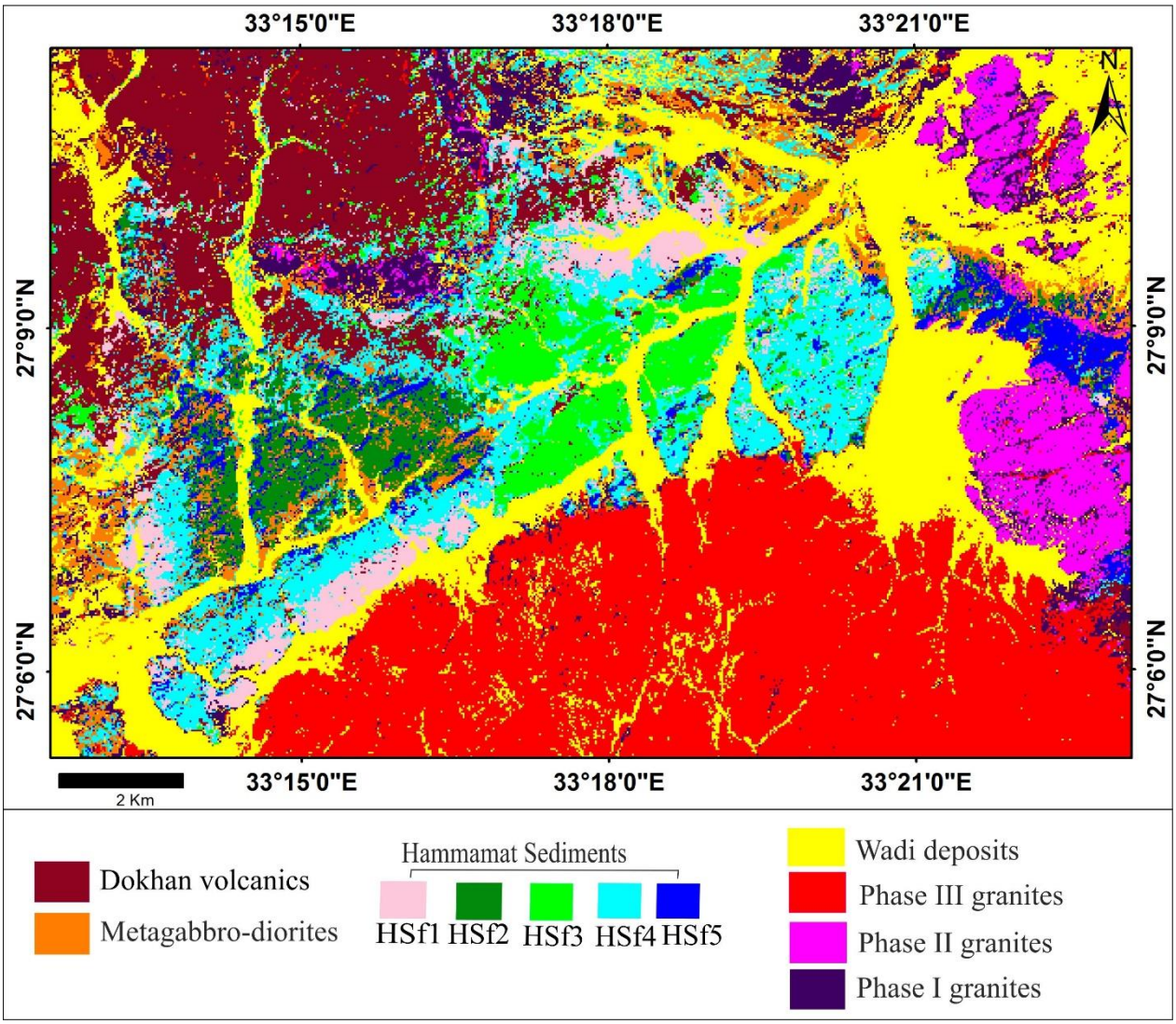

Figure 6. Lithological classification for the studied area using maximum likelihood classifier on Landsat-8.

4.2. Field verification and petrography

The RS data have separated the sediments into five distinct colors for different lithological packages, which resulted in the division of the HS into five facies units (HSf1, HSf2, HSf3, HSf4, HSf5), and identifying three types of granites (Phase I, Phase II, Phase III). These previously unmapped units were confirmed and identified using field observation in the manner described below.

HSf1 is a small outcrop along Wadi Bali. This unit is dominated by a brownish-gray poorly sorted matrix-supported conglomerate (with sandy matrix) and sandstone package. The conglomerate of this unit is composed of cobble to boulder-size grains (Figure 7a).

HSf2 is represented in the central west of the area characterized by a dominant green conglomerate and breccia (Figure 7b) with little gray sandstone. This facies unit is highly influenced by NE-trending dikes. The conglomerate is grain-supported with low percentage of sandy matrix. The grains are mostly elongated, angular to sub-rounded, and range in size from granular to cobble. It is polymictic type containing predominant greenish andesitic to dacitic volcanic fragments, laminated tuffs, and jasper, as well as foliated granites, green metasediments, chert, and reworked sediment fragments. These volcanic fragments are characterized by amygdaloidal and porphyritic textures.

HSf3 is represented in fine-grained dominant sediments at the center of the area. It consists of bedded to cross-bedded sandstones with thin ripples and gray laminated silty-mudstone interbeds (Figure 7c). The sandstone is dark green to a grayish color of graywacke type composed of quartz and feldspar set in a high percentage of a matrix (Figure 7d).

HSf4 includes a mixed gray sandstone and siltstone with conglomerate sediments. This unit is represented in the south of the studied area at the margin of the sedimentary basin, and is also recognized around HSf2 as sub-facies (HSf4a). The siltstones are more tilted and jointed. Near the contact with the Gattar granite, this siltstone performs as a barrier to the uranium-bearing solutions [47, 63]. Moreover, the conglomerate is gray, poorly sorted matrix-supported, and composed of pink granite fragments (Figure 7e). HSf4a sub-facies has the same lithological characteristics but not overlapping and its conglomerate is distinguished by grayish-green cobble grains followed by sand and silty-shale interlayered.

HSf5 is a small exposure setting between two granitic plutons of G.El Sala`at and G.El Reddha and scattered along the faults. This unit is distinguished by tuffaceous material and metamorphosed pelitic sediments during the intrusion of the younger granites and along the fault plane. The latter was identified by shearing and mylonitization near the fault plane. Other thermal metamorphoses comprise an abundance of quartz, feldspar, biotite, and a few cordierites. Cordierite is the characteristic metamorphic mineral in the innermost zone and biotite in the outermost zone forming porphyroblast and hornfels texture (Figure 7f).

The granite of the area can be classified into three phases. Phase I is small scattered granite in the north and east of the studied area (Figure 2a). It is characterized by reddish color, and fractures and dissected by intermediate to basic dikes (Figure 8a). These granites associated with dikes are more affected by the process of the alteration as epediotization and kaolinitization (Figure 8b). This granite contains quartz, plagioclase, alkali feldspar, and biotite crystals, and is classified as syenogranite to granodiorite. Phase II granite was represented in G. El Sala`at and G. El Reddha, which is accurately classified in the (6/5,5/4,4/3 RGB) band ratio as light-green false color. Exfoliation and an abundance of mafic xenoliths distinguish this granite (Figure 8c). It is composed primarily of orthoclase, oligoclase, perthite, albite, and quartz, which have been classified as syenogranite to monzogranite (Figure 8d).

Phase III is represented by G. Gattar. It is the youngest phase of granites that intruded the studied area and characterize by pink to reddish colors and high rigid mountains. This granitic batholith offshoot into HS, forming intrusive contact (Figure 8e). Later, the HS in the studied area was affected by intensive thrust faults being controlled partially with the granite/Hammamat contact. The Gattar granite is classified as alkali syenogranite to perthitic leucogranite petrographically, which primarily contains a high percentage of quartz, potassium-feldspar perthite (Figure 8f) and as meta-aluminous leucogranite, A-type granite geochemically [63]. Also it is specialized by the occurrence of uranium mineralization restricted to sheared tectonic contact between the HS and granite [64].

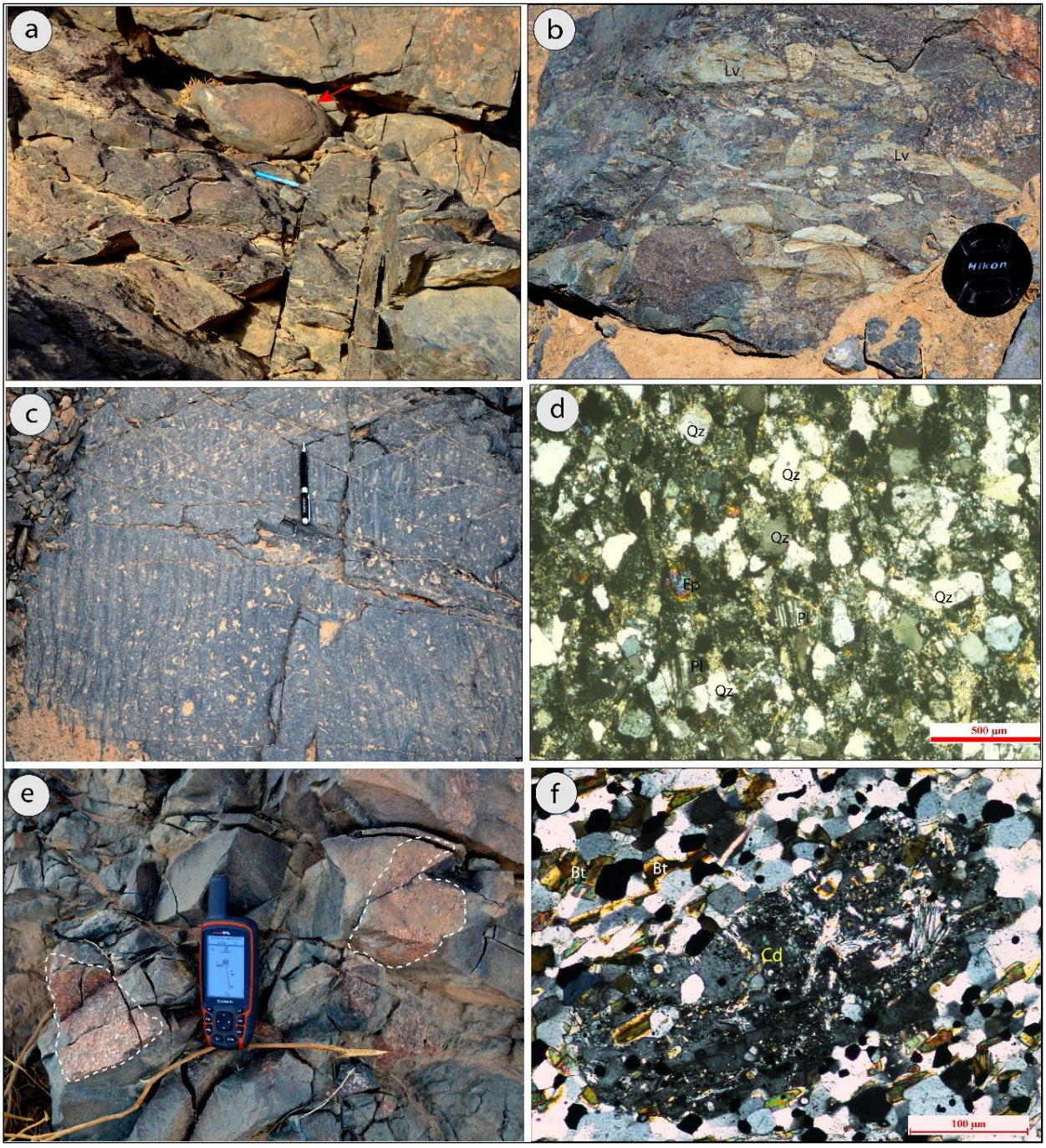

Figure 7. Field and petrographic photos of different facies of the Hammamat sediments (HSf) showing (a) Rounded boulder clasts (red arrow) in a brownish gray conglomerate of HSf1. (b) Green breccia with elongated lithic volcanic fragments (Lv) of HSf2. (c) Ripple marks in the graywacke sandstone in HSf3. (d) The main composition of graywacke is quartz (Qz), plagioclase (Pl) and epidote (Ep) embedded in a fine matrix at HSf3, CN. (e) Angular pink granite fragments in gray conglomerate of HSf4. (f) Porphyroblast of cordierite crystal (Crd) with Hornfels texture of biotite crystal (Bt) and quartz rich in HSf5, CN.

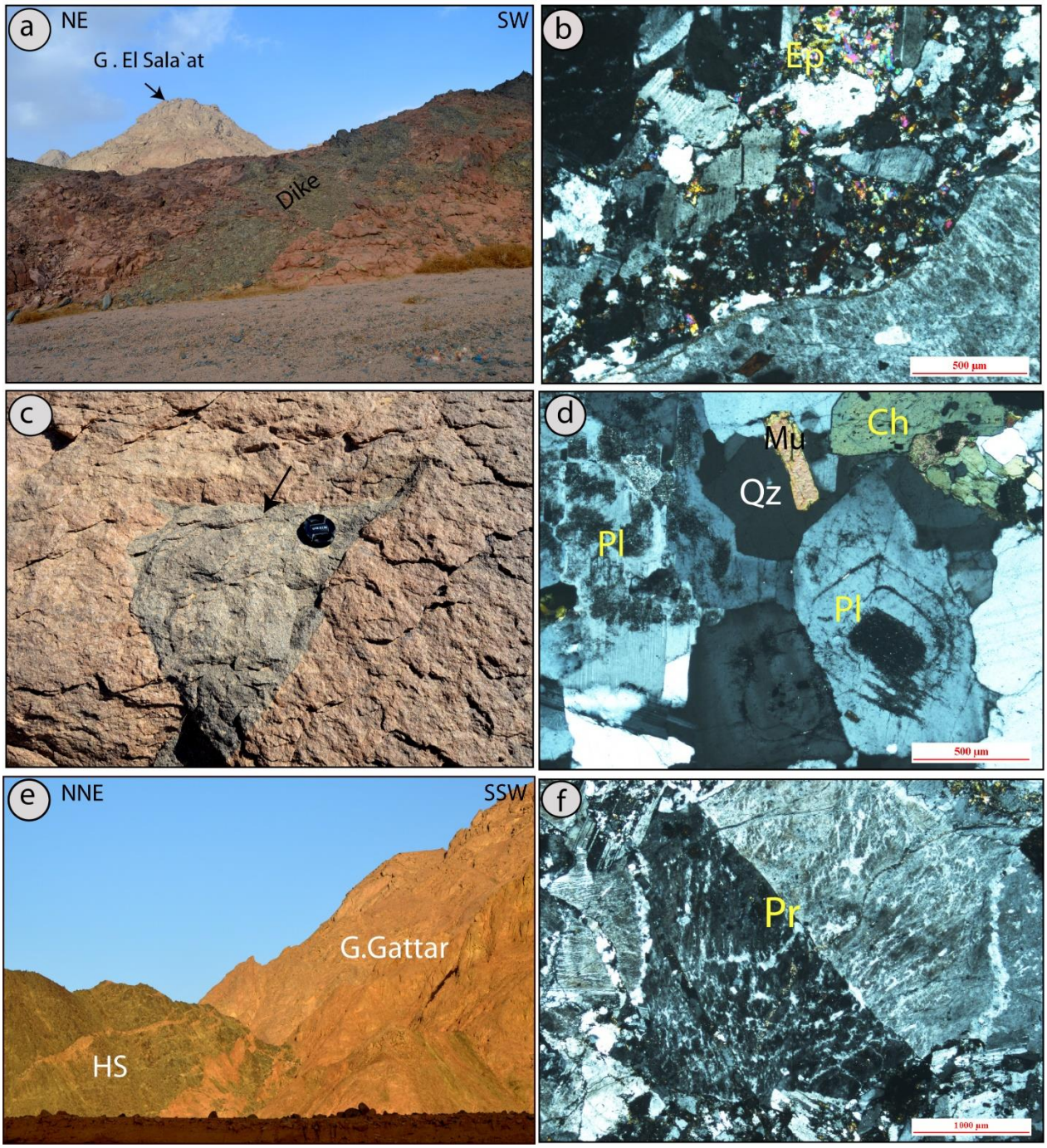

Figure 8. Field and petrographic photos of granite showing (a) Basic dikes intruded the phase I granite behind G.El Sala`at. b) Epidotization (Ep) process in granite along intruded dikes. (c) Mafic xenoliths in G.El Redhha. (d) Composition of second phase granite as quartz (Qz) plagioclase (Pl), muscovite (Mu) and biotite altered to chlorite (Ch) crystals, CN. (e) The intrusive contact of phase III granite into Hammamat sediments (HS). (f) Perthite crystal (Pr) in Gattarian granite, CN.

4.3. Lineament analysis

The lineaments analysis shows the linear features and their intensity in different parts of the region. This automatic lineament reveals several lines of structural identification that tend to be NE-trending dominant as well as NNE-SSW, and disclosed less influence on NW-SE orientation, as shown in the rose diagram (Figure 9). In the current region, the NNE dominant lineaments were formed advanced by rejuvenating the ENE-orientation fault that bounded the sediments. According to the density lineament map, the most of the lineaments are dense in the central and southern regions of the Umm Tawat area (Figure 9b).

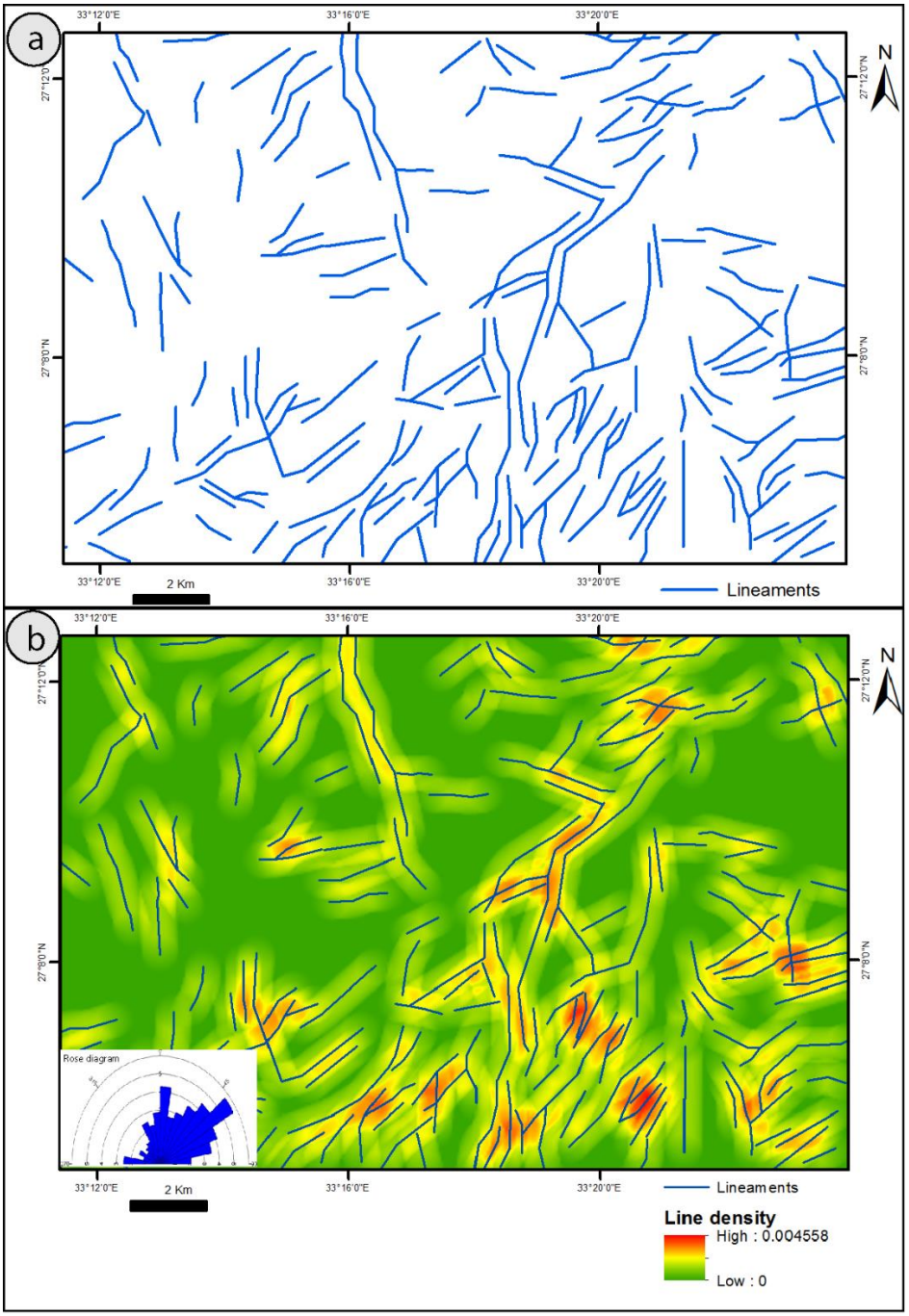

Figure 9. (a) Automatic lineaments extracted from the PC1 images. (b) Lineament density map with a rose diagram to show the main trends.

4.4. Structural features and geologic map of area

The area of investigation has been dissected by poly-phases of ductile and brittle deformation, leading to various structural elements, mainly folding, as well as distinct trends and types of faulting. Based on the variation of dipping beds, two major open anticline folds were detected within sediments nearly in the center of the area. The NE-oriented asymmetric plunged anticline fold (plunging toward the SW direction) with SE-dipping steep limb (55°) facing G.Gattar is developed to the southern part of the area (Figure 11). Another NE-oriented asymmetric plunged anticline (plunging toward the NE direction), the NW-dipping facing G. El Dokhan appears as monocline folds in G. Umm Tawat (Figure 2a). Also the minor folds are recorded with variably plunging axes (Figures 10a & 10b). The major faults constitute obvious lineaments on the lineament extracted images from image processing

(Figure 9), which reveal several trends of the faults and fractures. In various places in the area, some faults have been mapped, measured, and checked for kinematic indicators in the field like slickensides. Most of these faults have strike-slip movements through both the sinistral and dextral sense of displacement. They are more commonly recognized in the sediments and along the boundaries of the basin. The NE to ENE trending faults dominates, and shear zones exhibit an obvious dextral sense of movement. Several thrust faults follow this orientation dipping the SE direction (Figure 10c). These faults dissect most of the boundaries of different sedimentary facies units in the HS. The southern part of the sediments is bounded by the NE-striking thrust fault bringing the HS against the granitic contact HS (mainly HSf4) at the hanging wall of this thrust is 60° dipping toward the SE. The orientation of these faults and associated fold represent the Gulf-orthogonal fault and they developed in various tectonic phases. Most of the dike occurrences in the area follow this orientation. The sense of the detected movements revealed common sinistral faults striking towards the NNE-SSW and N-S Aqaba trend that was primarily districted along wadis in the eastern part of the basin, Moreover, local NNW-SSE dextral-slip faults observed in the western part as at W.Abu El Markh. This conjugate (NNW-SSE and N-S) trending faults were detected in the image processing of PC (Figure 4b).

High-resolution Google Earth images induced in Arc GIS to more accurately draw the boundary of lithologies by tracing the dike systems and homogenization of the supervised classification and structure of the area (Figure 11). Many lithological units have a new set of borders, and the others have been identified. As it turns out, the rock unit of the HS was reclassified as different facies units than before, and the granitoid was also discriminated against into three types.

The remote sensing manifested the tracing continuity of the bedding planes to outline the stratigraphic facies units. It also shows a group of discordant facies units in contact and around the basin center. This tracing is combined with detected structural elements to understand the relationship of these facies units with each others. They are arranged from the oldest in the basin (HSf1, HSf2, HSf4a, HSf3) at the center of the two folds the youngest HSf4, HSf5 at the margin of the basin. HSf4 and 5 are nearly concordant to SW and East at the marginal basin. The other main HSf units have structural and discordant boundaries and truncate each other. HSf3 truncates to HSf4 along NE-striking fault boundaries, HSf1 is situated at the core of the lower anticline fold, and has the structural boundary between their limbs and truncated to HSf4a with thrust fault and strike-slip faults in the south and western part of the basin respectively. HSf2 at the up dipping of the upper anticline fold, which appears as a triangular shape dissected by several dikes, the boundaries have a gradational topography with HSf4a in the west and thrust faults in the south. They were interleaved by Dokhan volcanics in the NW part of the basin.

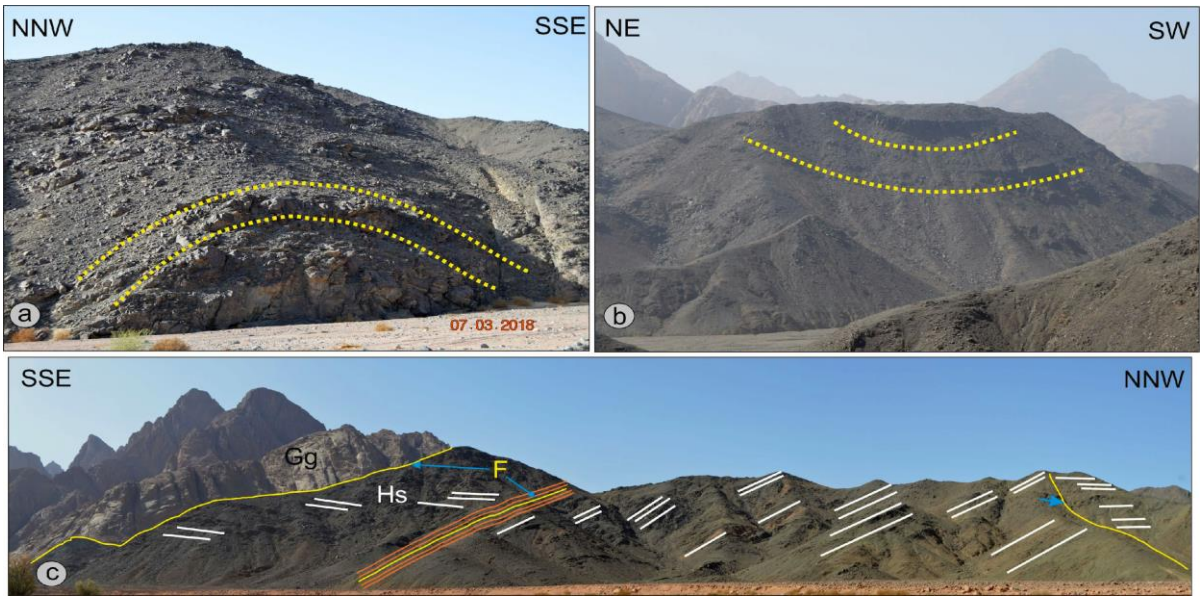

Figure 10. (a,b) Field photography showing anticline and syncline fold within Hammamat sediments respectively. (c) The panoramic view shows the variation of dipping beds within Hammamat sediment (HS) during several NE-trending thrust faults (F) and along the contact with Gattar granite (Gg).

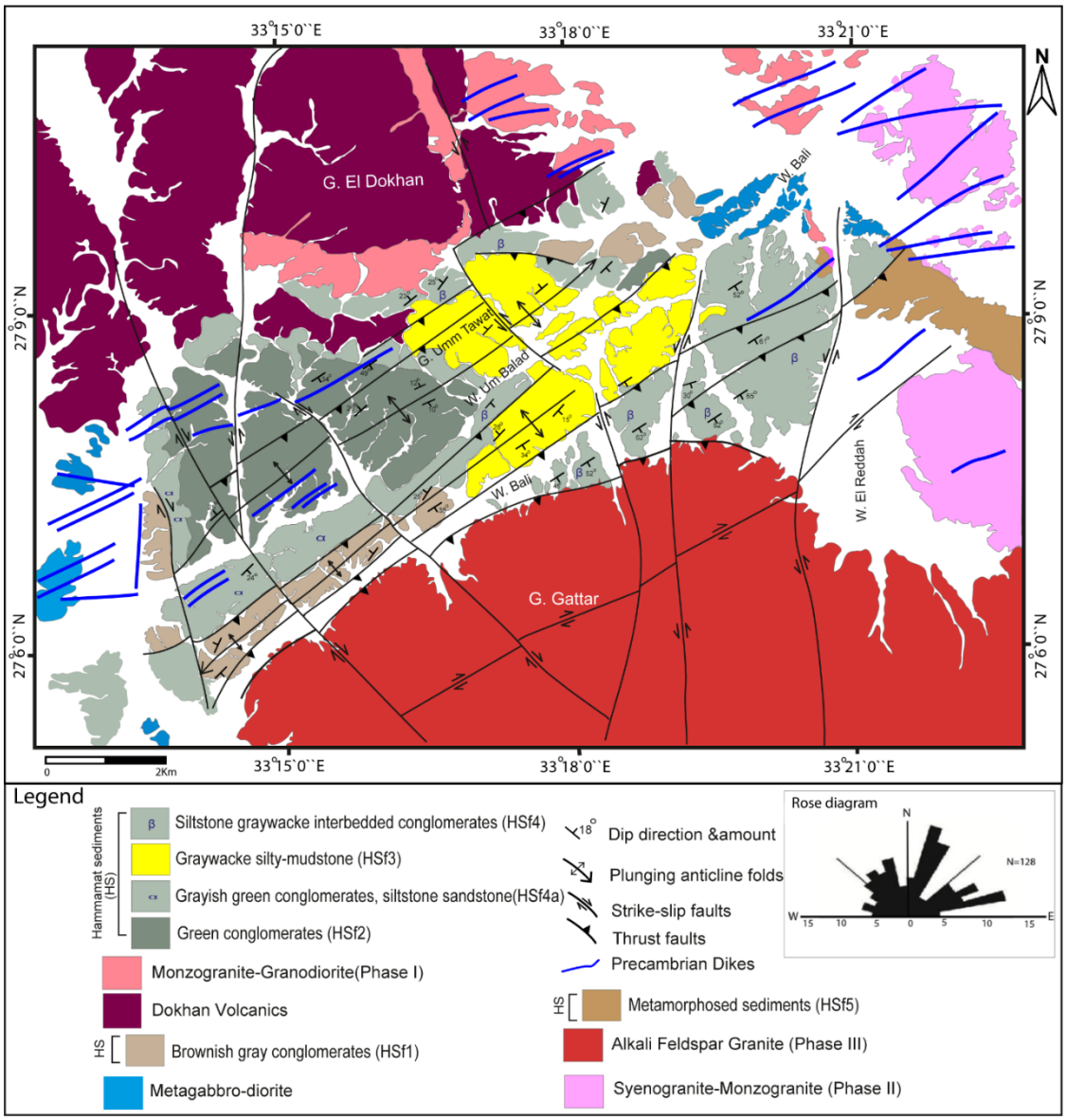

Figure 11. Update Geologic maps of the Umm Tawat area (based on the present study) and the Rose diagram illustrate the main strike frequency of faults.

5. Conclusions

The enhancement processing techniques of the Landsat-8 OLI data were executed in this work allowing the differentiation of the Precambrian rock assemblage of the Umm Tawat including various facies of Hammamat sediments and associated volcanics and intrusive units. Band ratios (6/5, 5/4, 4/3 RGB), and (4/2, 6/5, (7+6)/4 RGB), and PC1, PC2, PC3 were effective tools to discriminate Gattar granite from Sala`at El Bali and granitic intrusion in the north of the area, variant lithofacies within the Hammamat sediments and structural elements in the present study. The performed of the maximum likelihood supervised classification algorithm was efficient in digitizing the ten rock units to construct a new digital geologic map with an overall accuracy of 83%. The main detected structural lineaments by using PC1 of principal component analysis from OLI data and field observations indicate the dominance of the NE- and NNE-strike direction with subordinate NW-SE orientation. Finally, the field and petrographic verification of the remote sensing results discriminates five lithofacies of Hammamat sediments (HSf) including HSf1 brownish gray conglomerate and sandstone, HSf2 green conglomerate dominant containing mainly volcanic fragments, HSf3 fine-grained sediments of greywacke and silty mudstone, HSf4 interbedded conglomerates and siltstone with uranium enrichments related to the intrusive contact, and HSf5 as thermally metamorphosed pelitic sediments with recrystallized quartz, biotite, and cordierite minerals with porphyroblast and

hornfels textures. They also reveal three granite phases (phase I, II, III) that consist of monzogranite, syenogranite to alkaline syenogranite in the youngest phase as well as distinguishing between Dokhan volcanic and metagabbro-diorite. The recognized units of the Precambrian rock assemblage of Umm Tawat with the field, structural liniments, and high-resolution Google Earth image used as a separate layer create a new geologic map of the area with ten lithofacies units.

Acknowledgments

The first author would like to acknowledge and express gratitude to the geology department at Cairo University for funding the present study. Thanks extend to Dr. Khamis Farhoud consultant geophysicist, Dr. Hossam Khamis at nuclear material authority, and my colleague A. Hammam at Cairo University for field and technical support.

References

[1]. Crosta, A. P. and Rabelo, A. (1993). Assessing of Landsat TM for hydrothermal alteration mapping in central-western Brazil. Proceedings of Ninth Thematic conference geologic remote sensing Pasadinea, California, USA. 1053-61.

[2]. Shokry, M.M., Sadek, M.F., Osman, A.F., and El Kalioubi, B.A. (2021). Precambrian basement rocks of Wadi-Khuda-Shut area, South Eastern Desert of Egypt: Geology and remote sensing analysis. Egyptian Journal of Remote Sensing and Space Science. 24 (1): 59–75.

[3]. Hassan, S.M., El kazzaz, Y.A., Taha, M.M.N., and Mohammad, A.T. (2017). Late Neoproterozoic basement rocks of Meatiq area, Central Eastern Desert, Egypt: Petrography and remote sensing characterizations. Journal of African Earth Sciences. 131:14–31.

[4]. Kumar, C., Shetty, A., Raval, S., Sharma, R., and Ray, P.K.C. (2015). Lithological Discrimination and Mapping using.

[5]. Pandey, P. and Sharma, L.N. (2019). Image Processing Techniques Applied to Satellite Data for Extracting Lineaments Using PCI Geomatica and Their Morphotectonic Interpretation in the Parts of Northwestern Himalayan Frontal Thrust. Journal of the Indian Society of Remote Sensing. 47 (5): 809–820. https://doi.org/10.1007/s12524-019-00962-2

[6]. Sadek, M.F. and Hasan, S.M. (2012). Application of remote sensing in lithological discrimination and geological mapping of precambrian basement rocks in the eastern desert of Egypt. 33rd Asian Conference on Remote Sensing 2012, ACRS 2012. 1:362–371.

[7]. Sabins, F.F. (1997).“Remote Sensing principles and interpretation,” W. H. Free. Company, New York, pp. 366–371.

[8]. Qari, M.H.T., Madani, A.A., Matsah, M.I.M., and Hamimi, Z. (2008). “Utilization of Aster and Landsat Data in Geologic Mapping of Basement Rocks of Arafat Area, Saudi Arabia.” Arabian Journal for Science and Engineering. 33 (1 C): 99–116.

[9]. Amusuk, D.J., Hashim, M., Pour, A.B., and Musa, S.I. (2016). Utilization of landsat-8 data for lithological mapping of basement rocks of plateau state north central Nigeria. International Archives of the Photogrammetry, Remote Sensing and Spatial Information Sciences - ISPRS Archives. 42 (4W1): 335–337. https://doi.org/10.5194/isprs-archives-XLII-4-W1-335-2016.

[10]. Abdeen, M., Thurmond, A.K., Abdelsalam, M., and Stern, B. (2001). Application of ASTER band-ratio images for geological mapping in arid regions; The Neoproterozoic Allaqi Suture. Egypt. Geol. Soc. Am. 33:1–289.

[11]. Fowler, A., Baghdady, A., Abdelmalik, K., and Gad, A. (2020). Remote sensing-guided stratigraphic dissection of an Ediacaran terrestrial molasse basin (Kareim basin, Egypt), with implications for sedimentary evolution. Precambrian Research. 338:105589.

[12]. Gad, S. and Kusky, T. (2006). Lithological mapping in the Eastern Desert of Egypt, the Barramiya area, using Landsat thematic mapper (TM). Journal of African Earth Sciences. 44 (2): 196–202.

[13]. Hamimi, Z., Hagag, W., Kamh, S., and El-Araby, A. (2020). Application of remote-sensing techniques in geological and structural mapping of Atalla Shear Zone and Environs, Central Eastern Desert, Egypt. Arabian Journal of Geosciences. 13 (11).

[14]. Hassan, S.M. and Sadek, M.F. (2017). Geological mapping and spectral based classification of basement rocks using remote sensing data analysis: The Korbiai-Gerf nappe complex, South Eastern Desert, Egypt. Journal of African Earth Sciences. 134(July):404–418.

[15]. Kamel, M., Youssef, M., Hassan, M., and Bagash, F. (2016). Utilization of ETM+ Landsat data in geologic mapping of wadi Ghadir-Gabal Zabara area, Central Eastern Desert, Egypt. Egyptian Journal of Remote Sensing and Space Science. 19 (2): 343–360.

[16]. Seleim, A.M. and Hammed, M.S. (2016). Applications of remote sensing in lithological mapping of east esh el malaha area, southwest gulf of suez - egypt. International Journal of Scientific & Engineering Research. 7 (12): 691–701.

[17]. Abd El-Fatah, A.A.E., Madani, A.A., Surour, A.A.A., and Azer, M.K. (2023). Integration of Landsat-8 and Reflectance Spectroscopy data for Mapping of Late Neoproterozoic Igneous Ring Complexes in an Arid Environment :a Case Study of Gebel El-Bakriyah

Area, Eastern Desert, Egypt. 14 (1): 13–31.

[18]. Ali-Bik, M. W., Sadek, M. F., and Hassan, S. M. (2022). Basement rocks around the eastern sector of baranis-aswan road, Egypt: Remote sensing data analysis and petrology. Egyptian Journal of Remote Sensing and Space Science. 25 (1): 113–124.

[19]. Qasim, M. Khan, S. D. Haider, R., and Rasheed M. (2022). Integration of multispectral and hyperspectral remote sensing data for lithological mapping in Zhob Ophiolite, Western Pakistan, Arabian Journal of Geosciences. 15 (7): 1–19.

[20]. Anwar, M., Abu El-Leil, I., and Salem, S.M. (2023). Lithological and Alteration Mapping at the Um El-Rus Area, Central Eastern Desert, Egypt, Using Remote Sensing Techniques', Journal of the Indian Society of Remote Sensing, 0123456789.

[21]. Hammed, M. S. and Abdel Khalek, A. (2015). Section Name. 15th International SGEM GeoConference. I: 11–22.

[22]. Hammam, A., Gaber, A., Abdelwahed, M., and Hammed, M. S. (2020). Geological mapping of the Central Cairo-Suez District of Egypt, using space-borne optical and radar dataset. Egyptian Journal of Remote Sensing and Space Science. 23 (3): 275–285.

[23]. Sayed, F., Hammed, M.S., Shided, A.G., and Hussein, A.W. (2023). Implementation of the remote sensing techniques in the structural and lithological mapping of the northwestern margin of the Red Sea , Egypt, Journal of Mining and Environment, in press.

[24]. Stern, R.J. (1994). Arc assembly and continental collision in the Neoproterozoic East African Orogen: implications for the consolidation of Gondwanaland. Annual Review of Earth & Planetary Sciences. 22: 319–351.

[25]. Abdeen, M.M. and Greiling, R.O. (2005). A quantitative structural study of late Pan-African compressional deformation in the Central Eastern Desert (Egypt) during Gondwana assembly. Gondwana Research. 8 (4): 457–471.

[26]. Johnson, P.R., Andresen, A., Collins, A. S., Fowler, A.R., Fritz, H., Ghebreab, W., Kusky, T., and Stern, R.J. (2011). Late Cryogenian-Ediacaran history of the Arabian-Nubian Shield: A review of depositional, plutonic, structural, and tectonic events in the closing stages of the northern East African Orogen. Journal of African Earth Sciences. 61 (3): 167–232.

[27].Johnson, P. and Woldehaimanot, B. (2003). Development of the Arabian-Nubian Shield: Perspectives on accretion and deformation in the northern East African Orogen and the assembly of Gondwana. Geological Society, London, Special Publications. 206: 289–325.

[28]. Abd El-Rahman, Y., Polat, A., Fryer, B. J., Dilek, Y., El-Sharkawy, M., and Sakran, S. (2010). The provenance and tectonic setting of the Neoproterozoic Um Hassa Greywacke Member, Wadi Hammamat area, Egypt: Evidence from petrography and geochemistry. Journal of African Earth Sciences. 58 (2): 185–196.

[29]. El-Gameel, K. (2018). The Ediacaran volcanosedimentary succession of Gabal Abu Had, North Eastern Desert, Egypt: geological study, facies analyses, and depositional setting. Arabian Journal of Geosciences. 11(8).

[30]. Eliwa, H.A., Kimura, J.I., and Itaya, T. (2006). Late Neoproterozoic Dokhan Volcanics, North Eastern Desert, Egypt: Geochemistry and petrogenesis. Precambrian Research. 151 (1–2): 31–52.

[31]. Willis, K.M., Stern, R.J., and Clauer, N. (1988). Age and geochemistry of late precambrian sediments of the hammamat series from the Northeastern desert of Egypt. Precambrian Research. 42 (1–2): 173–187.

[32]. Stern, R.J., Gottfried, D., and Hedge, C.E. (1984). Late Precambrian rifting and crustal evolution in the Northeastern Desert of Egypt. Geology. 12 (3): 168–172.

[33]. Eliwa, H. Breitkreuz, C., Khalaf, I., and El Gameel, K. (2010). Depositional styles of Early Ediacaran terrestrial volcanosedimentary succession in Gebel El Urf area, North Eastern Desert, Egypt. J. African Earth Sci. 57 (4): 328–344.

[34]. Conoco, (1987). Egyptian General Authority for Petroleum (UNESCO Joint Map Project), 20 Sheets, Scale 1500 000, Cairo.

[35]. Dardir, A.A. and Abu Zeid, K. (1972). Geology of the basement rocks between latitudes 27° 00 and 27 30° N, Eastern Desert. Annual Geology Survey. 2:129–158.

[36]. El Ramly, M.F. (1972). A new geological map for the basement rocks in the Eastern and South- Western deserts of Egypt, scale 1:1,000,000. Annual Geology Survey. 2:1–8.

[37]. Ghobrial, M.G. and Lotfi, M. (1967). The Geology of Gebel Gattar and Gebel Dokhan Areas. Geological Survey of Egypt. 40.

[38]. EGSMA (2002). Geologic Map of Marsa Sha`ab Quadrangle, Egypt, Scale 1:250.000.

[39]. Greenberg, J.K. (1981). Characteristics and origin of Egyptian Younger Granites. Bulletin of the Geological Society of America. 92(5 PART2): 749–840.

[40]. Ghoneim, M.F., Lebda, E.M., Abu Anbar, M.M., and Abd El-Wahed, M.A. (2007). Toward a New Concept for the Classification of Granitic Rocks of the Eastern Desert, Egypt: Geothermobarometry Constraints. The Fifth International Conference on the Geology of Africa. 142 (1): 131–142.

[41]. Frost, B.R., Barnes, C.G., Collins, W.J., Arculus, R.J., Ellis, D.J., and Frost, C.D. (2001). A geochemical classification for granitic rocks. Journal of Petrology. 42 (11): 2033–2048.

[42]. El-Sayed, M.M., Mohamed, F.H., Furnes, H., and Kanisawa, S. (2002). Geochemistry and petrogenesis of the neoproterozoic granitoids in the central Eastern Desert, Egypt. Chemie Der Erde. 62 (4): 317–346.

[43]. El-Naby, H.H.A. (2021). The Egyptian Granitoids: an up-to-date Synopsis (Z. Hamimi et al. (Ed.); Issue September). The Geology of the Egyptian Nubian Shield, Regional Geology Reviews Springer Nature Switzerland.

[44]. Noweir, A.M., Sewifi, B.M., and Abu El Ela, A.M. (1990). Geology, petrography, geochemistry and petrogenesis of the Egyptian younger granites. Qatar University Science Bulletin. 10:363 – 393.

[45]. Wilde, S.A. and Youssef, K. (2002). A re-evaluation of the origin and setting of the late precambrian Hammamat group based on SHRIMP U-Pb dating of detrital zircons from Gebel Umm Tawat, north eastern Desert, Egypt. Journal of the Geological Society. 159 (5): 595–604.

[46]. Akaad, M. and Noweir, A.M. (1969). Lithostratigraphy of the Hammamat-Um Seleimat district, Eastern Desert, Egypt. Nature. 223:284–285.

[47]. Dessouky, O.K., Dardier, A.M., and Abdel Ghani, I.M. (2019). Egyptian Hammamat molasse basins and their relations to arc collision stages: Implications for radioactive elements mineralization potential. Geological Journal. 54 (3): 1205–1222.

[48]. Khalifa, A.A., Khamis, H.A., El-Sayed, M.M., and Shalaby, M.H. (2020). Geology and evolutionary stages of the Late Precambrian Hammamat sediments at Gebel Um Tawat, North Eastern Desert, Egypt. Arabian Journal of Geosciences. 13 (12): 1–19.

[49]. Yousefi, M. and Hronsky, J.M.A. (2023) 'Translation of the function of hydrothermal mineralization-related focused fluid flux into a mappable exploration criterion for mineral exploration targeting', Applied Geochemistry, 149.

[50]. Stern, R.J., Sellers, G., and Gottfried, D. (1988). Bimodal dike swarms in the North Eastern Desert of Egypt: significance for the origin of late Precambrian "A - type" granites in northern Afro -Arabia. In: El Gaby S, Greiling RO (eds) The Pan-African belt of Northeast Africa and Adjacent Areas, Vieweg, p (E. G. S & G. RO (eds.)). The Pan-African belt of Northeast Africa and Adjacent Areas, Vieweg.

[51]. Beyth, M., Eyal, Y., and Garfunkel, Z. (2014). The geology of the northern tip of the Arabian-Nubian shield. Journal of African Earth Sciences. 99 (PA2):332–341.

[52]. Stern, R.J., Gottfried, D., and Hedge, C.E. (1984). Late Precambrian rifting and crustal evolution in the Northeastern Desert of Egypt. Geology. 12(3):168–172.

[51]. Liu, J.G. and Mason, P.J. (2016). Image Processing and GIS for Remote Sensing: Techniques and Applications. John Wiley and Sons, Ltd; Chichester, UK: Inverse distance weighted average.

[53]. Wolters, J., Goldin, L., Watts, D. R., and Harris, N. B. W. (2005). Remote sensing of gneiss domes and granite in southern Tibet /. Geol Soci Am(Abstr Program). 37 (5): 93.

[54]. Richards, J.A. and Jia, X. (1999). Remote Sensing Digital Image Analysis. In Remote Sensing Digital Image Analysis.

[55]. CCRS. (1999). Canada Center of Remote Sensing, Fundamentals of Remote Sensing, Forestry.

[56]. Chen, S. and Rao, P. (2009). Regional land degradation mapping using MODIS data and decision tree (DT) classification in a transition zone between grassland and cropland of northeast China. Information Science and Engineering (ICISE),1st International Conference on. IEEE.

[57]. Solomon, S. and Ghebreab, W. (2006). Lineament characterization and their tectonic significance using Landsat TM data and field studies in the central highlands of Eritrea. Journal of African Earth Sciences. 46 (4): 371–378.

[58]. Adhab, S.S. (2019). Lineament automatic extraction analysis for Galal Badra river basin using Landsat 8 satellite image. Iraqi Journal of Physics. 12 (25): 44–55.

[59]. Ahmadi, H. and Pekkan, E. (2021). Fault-based geological lineaments extraction using remote sensing and gis—a review. Geosciences (Switzerland). 11 (5).

[60]. Hung, L. Q., Batelaan, O., and De Smedt, F. (2005). Lineament extraction and analysis, comparison of LANDSAT ETM and ASTER imagery. Case study: Suoimuoi tropical karst catchment, Vietnam. Remote Sensing for Environmental Monitoring, GIS Applications, and Geology.

[61]. Mah, A., Taylor, G. R., and Balia, L. (1995). Lineament anlysis of Landsat Thematic Mapper images, Northern Territory, Australia. 61 (6): 761–773.

[62]. Goetz, A.F.H. and Rowan, L.C. (1981). Geologic Remote Sensing. Science. 211(4484):781–791.

[63]. El-Kammar, A.M., Salman, A.E., Shalaby, M.H., and Mahdy, A.I. (2001). Geochemical and genetical constraints on rare metals mineralization at the central Eastern Desert of Egypt. Geochemical Journal. 35 (2): 117–135.

[64]. Salman, A.B., Shalaby, M.H., Ragab, M.M., and AbuZaid, A. (1996). Relation Between Uranium Mineralization and Structural Features, Gebel Gattar, North Eastern Desert, Egypt. Nuclear Material Authority. 9–13.

کاربرد سنجش از دور در نقشه برداری سنگ شناسی مجموعه سنگ پرکامبرین ام طوات، صحرای شمال شرقی، مصر

کمر سمیر*، محمد الشرکاوی، احمد نیازی البرکوکی و محمد صالح حامد

گروه زمین شناسی، دانشکده علوم، دانشگاه قاهره، مصر

ارسال ۲۰۲۳/۰۳/۱۷، پذیرش ۲۰۲۳/۰۴/۱۳

* نویسنده مسئول مکاتبات: moonsamir9@cu.edu.eg

چکیده:

مجموعه‌های سنگی پرکامبرین ناحیه ام طوات در صحرای شمال شرقی مصر دارای یک پرتودهی با گرایش ENE متمایز از رسوبات حمامات (HS) بین توده گرانیتی گبل گاتار و جانشینی آتشفشان‌آواری جبل الدخان هستند. کار حاضر داده‌های Landsat-8 و تکنیک‌های پردازش تصویر مانند امضای طیفی، تجزیه و تحلیل مؤلفه‌های اصلی، کشش همبستگی، و نسبت‌های باند را برای نقشه‌برداری از واحدهای مختلف سنگ پرکامبرین و رخساره‌های سنگی HS و تماس‌های زمین‌شناسی آن‌ها به کار می‌گیرد. واحدهای قابل نقشه برداری شناسایی شده از این مجموعه به طور کامل با امضای طیفی، تأیید میدانی، تجزیه و تحلیل خطی و توصیف سنگ نگاره آنها شناسایی می‌شوند. نقشه سنگ‌شناختی با وضوح بالا بر اساس الگوریتم حداکثر احتمال، ده واحد کاملاً تفکیک‌پذیر از واحدهای رخساره‌های سنگی گرانیتوئیدی و HS جوان‌تر را در کنار واحدهای سنگ‌های آتشفشانی دخان و متاگابرو-دیوریت نشان می‌دهد. پنج واحد رخساره HS شناسایی شده عبارتند از کنگلومرا خاکستری مایل به قهوه‌ای و ماسه سنگ HSf1، یک کنگلومرا سبز با قطعات آتشفشانی غالب HSf2، رسوبات ریزدانه خاکستری و گلسنگ سیلتی HSf3، کنگلومراهای بین لایه‌ای و کنگلومراهای غنی از سیلتروس در تماس با u. رسوبات پلیتیک دگرگون شده حرارتی HSf5. تکنیک‌های سنجش از دور برای اولین بار برای آشکار کردن تغییرات رخساره‌ای دقیق رسوبات حمامات ام طوات استفاده شده است. در نهایت، نتایج فوق الذکر به پایگاه داده Arc GIS برای به روز رسانی نقشه زمین شناسی با مرزهای دقیق واحد سنگ وارد می شود.

کلمات کلیدی: سنجش از دور، تبعیض سنگ شناسی، رسوبات همامات، ام طوات.